ADVANCED OPTICAL MATERIALS
www.advopticalmat.de

Gate-Switchable Photovoltaic Effect in BP/$MoTe_2$ van der Waals Heterojunctions for Self-Driven Logic Optoelectronics

Siqi Hu, Jinpeng Xu, Qinghua Zhao, Xiaoguang Luo, Xutao Zhang, Tao Wang, Wanqi Jie, Yingchun Cheng, Riccardo Frisenda, Andres Castellanos-Gomez, and Xuetao Gan**

Recently, van der Waals heterojunction based on 2D materials emerges as a promising technology for optoelectronic integrated circuits. Here, a self-driven optoelectronic logic device is demonstrated based on vertically stacked van der Waals heterojunction of black phosphorus and molybdenum telluride. Through the electrostatic doping by gating, the heterojunction is dynamically tuned to isotype (p-P and n-N) and anisotype (p-N) while the built-in electric field in the heterojunction is greatly changed. Consequently, the photovoltaic effect in the heterojunction is switchable by the gate voltage, enabling a novel self-driven optoelectronic logic element without the need of external biasing. This optoelectronic logic device shows promising characteristics of output dark current <1 pA, on/off current ratio >10^5, switching time <10 µs, broadband operation in the spectral range from 400 to 1600 nm, and linearly adjustable output current. The results may open up unprecedented opportunities to employ van der Waals heterojunctions for exploring logic optoelectronics with high performance and low power consumption.

1. Introduction

Growing number of transistors on the chip leads to a serious data transmission rate bottleneck in chip-to-chip electrical communications, known as the pin count limitation in electronic circuits.[1,2] Optoelectronic circuits can use the entire chip area for inter-chip communication through optical interconnects, providing high-speed and low-loss data transmissions in data centers and high-performance computing infrastructure.[3–5] Optoelectronic logic devices are important elements in optoelectronic circuits, which perform logical processing with optical signals and electrical signals.[6–10] Compared to traditional electrical logic devices, optoelectronic logic devices achieve both fast operating speed and large bandwidth,[11] and the non-interference between the optical input and the electrical input ensures parallel information detection and processing.[12–14]

In the past decades, various optoelectronic logic devices have been demonstrated based on materials including silicon, gallium nitride, and carbon nanotubes, etc.[15–17] These optoelectronic logic devices control the trapping and de-trapping of photogenerated carriers by the gate voltage to realize the logic switching of the output photocurrent. Unfortunately, the architecture of these devices hinders the great improvement of their performances. First, external electrical biases are required to transfer the photo-generated carriers, which inevitably give rise to large dark currents and extra power consumption.[18] Second, due to the trapping effect of defects, it is difficult to ensure the linear response of the photoelectric conversion.[19] Third, the trapping and de-trapping of photo-generated carriers are remarkably slow processes, which limit the operation speed of the optoelectronic logic devices in the timescale of seconds.[17,18,20]

In this work, we demonstrate a self-driven optoelectronic logic device based on a van der Waals heterojunction consisting of 2D black phosphorus (BP) and molybdenum telluride ($MoTe_2$). Different from the previously reported works,[15–18,21] the logic switch of this device relies on the modulation of the

S. Hu, Dr. X. Zhang, Prof. X. Gan
MOE Key Laboratory of Material Physics and Chemistry
under Extraordinary Conditions
and Shaanxi Key Laboratory of Optical Information Technology
School of Physical Science and Technology
Northwestern Polytechnical University
Xi'an 710129, China
E-mail: xuetaogan@nwpu.edu.cn
J. Xu, Dr. X. Luo, Prof. Y. Cheng
Shannxi Institute of Flexible Electronics
Northwestern Polytechnical University
Xi'an 710129, China
E-mail: iamxgluo@nwpu.edu.cn
Q. Zhao, Prof. T. Wang, Prof. W. Jie
State Key Laboratory of Solidification Processing
Northwestern Polytechnical University
Xi'an 710072, China
Q. Zhao, Dr. R. Frisenda, Dr. A. Castellanos-Gomez
Materials Science Factory
Instituto de Ciencia de Materials
de Madrid (ICMM-CSIC)
Madrid E-28049, Spain
The ORCID identification number(s) for the author(s) of this article can be found under https://doi.org/10.1002/adom.202001802.

DOI: 10.1002/adom.202001802

photovoltaic effect in the BP/$MoTe_2$ heterojunction. Thanks to the ambipolar conduction characteristics of the BP and $MoTe_2$,[22–24] the BP/$MoTe_2$ heterojunction can be tuned to anisotype (p-N) and isotype (p-P and n-N) by the gate voltage for reconfiguring the photovoltaic effect. Meanwhile, the photovoltaic effect converts optical signals into current signals without external bias, which has been proven to be a practical and sustainable self-driven solution for low-energy consumption optoelectronic devices.[25–27] As a result, with an optical signal as the "input" and a gate voltage as the "control," the photovoltaic current "output" of the BP/$MoTe_2$ heterojunction could be switched to perform a self-driven optoelectronic logic function. This fabricated optoelectronic logic device presents the decent performance of output dark current <1 pA, on/off current ratio >10^5, switching time < 10 µs, broadband operation in the spectral range from 400 to 1600 nm, and linearly adjustable output current signal. Our work promises the potential of van der Waals heterojunctions in self-driven optoelectronic logic devices for high-performance and low-power consumption optoelectronic circuits.

2. Results and Discussions

Figure 1a schematically illustrates the device configuration, in which the BP/$MoTe_2$ heterojunction was fabricated on a p-doped Si substrate coated with a 300 nm thick SiO_2 film. To make the vertically stacked BP/$MoTe_2$ heterojunction, a BP layer was first mechanically exfoliated onto a polydimethylsiloxane (PDMS) film and dry transferred onto the SiO_2/Si substrate.[28] In the same way, a $MoTe_2$ layer was precisely transferred onto the BP layer to overlap at the center of their channels. The gate voltage V_G was applied through the Si end to adjust the carrier densities in both BP and $MoTe_2$ layers. As a typical device shown

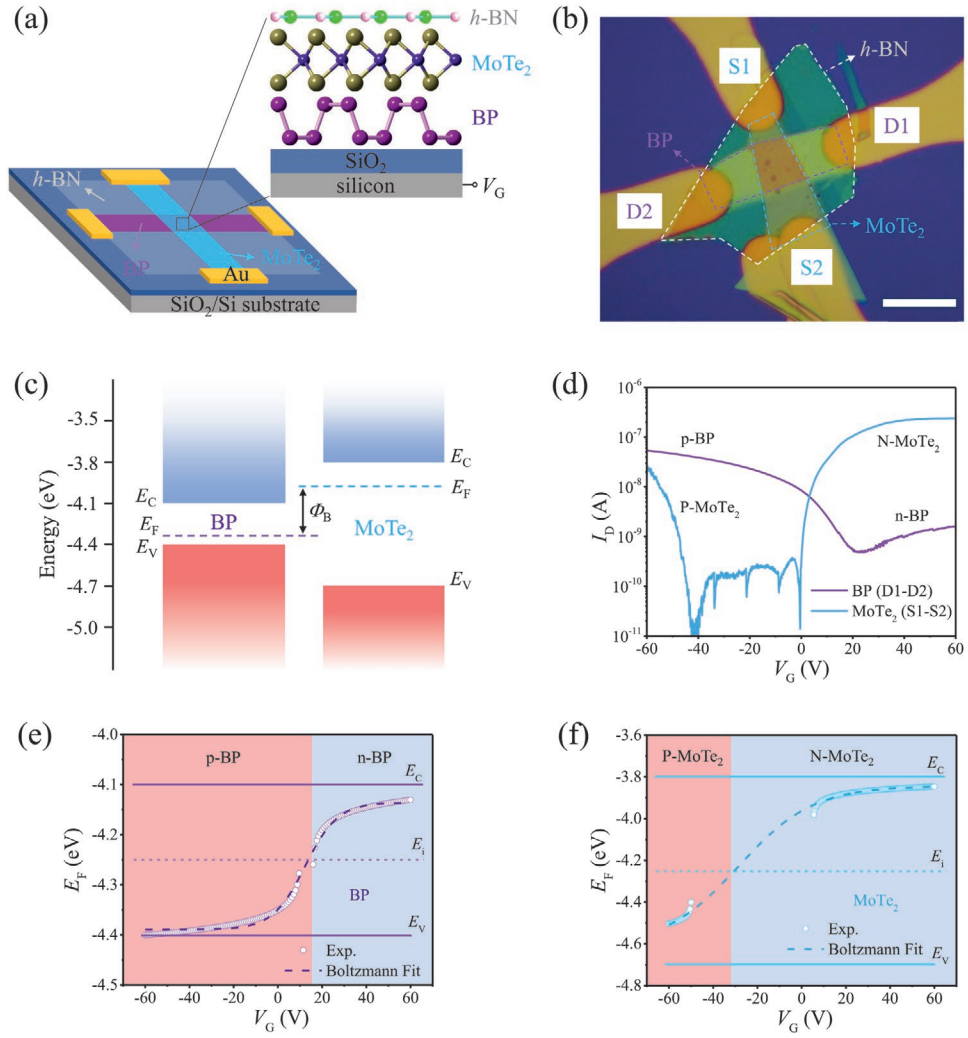

Figure 1. a) Schematic diagram of the vertically stacked van der Waals BP/$MoTe_2$ heterojunction device with lateral Au contacts. A top *h*-BN layer is used for the passivation. b) Optical microscope image of the fabricated device, where D1 and D2 (S1 and S2) indicate the metal contacts for the BP ($MoTe_2$) channel. Scale bar: 40 µm. c) Band profile of the BP and $MoTe_2$ layer. Built-in electric potential Φ_B of the heterojunction is equal to the Fermi level position difference between BP and $MoTe_2$. d) Ambipolar transport characteristics of the BP channel (purple curve, measured between D1 and D2) and the $MoTe_2$ channel (blue curve, measured between S1 and S2) at the bias-voltage 0.1 V. e,f) Electrostatic gate-dependent tuning of the Fermi level position in e) BP and f) $MoTe_2$. The intrinsic Fermi level positions E_i of BP and $MoTe_2$ are indicated.

in Figure 1b, both the BP and $MoTe_2$ thin layers are in contact with two 100 nm thick Au electrodes, forming a BP channel (between D1 and D2) and a $MoTe_2$ channel (between S1 and S2). Finally, the heterojunction was fully encapsulated with a thin *h*-BN flake to prevent the degeneration from environment[29] (more details about the device fabrication are provided in the Experimental Section). The thicknesses of the BP and $MoTe_2$ layers are ≈15 and ≈23 nm, respectively, as identified by the atomic force microscope in Figure S1 (Supporting Information). Raman spectroscopy was further performed to confirm the high quality of the BP layer, $MoTe_2$ layer, and heterojunction region in Figure S2 (Supporting Information).

Figure 1c shows the energy band diagrams of BP and $MoTe_2$. The bandgap and electron affinity of BP ($MoTe_2$) are ≈0.3 eV (≈0.9 eV) and ≈4.1 eV (≈3.8 eV), respectively.[30,31] The differences in bandgaps and electron affinities result in the BP/$MoTe_2$ heterojunction with a conduction band offset $\Delta E_C \approx 0.3$ eV and a valence band offset $\Delta E_V \approx 0.3$ eV. Figure 1d shows transfer characteristic curves of the BP channel (measured between D1 and D2) and $MoTe_2$ channel (measured between S1 and S2). When the gate voltage V_G sweeps from −60 to 60 V, the current of the BP channel performs ambipolar with a positive neutral point, indicating that the BP layer is intrinsically p-doped. The $MoTe_2$ channel also exhibits similar ambipolar conduction behavior and is intrinsically N-doped. The transfer characteristics of these two channels are consistent with the reports for individual BP and $MoTe_2$ correspondingly,[22,23] implying the heterojunction region almost does not affect the conduction of each channel. Therefore, the BP/$MoTe_2$ heterojunction can be tuned to isotype (p-P and n-N) and anisotype (p-N) configurations by the gate voltage.

To reveal more details about the built-in electric field in the BP/$MoTe_2$ heterojunction, we calculated the Fermi level positions of the two channels under different gate voltages. Based on the transfer characteristics, majority carrier concentrations for the BP channel can be estimated by

$$n/p = \frac{C_G|V_T - V_G|}{qt} \tag{1}$$

where q is the elementary charge, t is the thickness of BP, $C_G = 1.15 \times 10^{-8}$ F cm^{-2} is the capacitance of the 300-nm-thick SiO_2 gate oxide layer, and V_T is the threshold voltage for holes and electrons accordingly.[32] This formula can also be used for the $MoTe_2$ channel, because of capacitance for $MoTe_2$ around the heterojunction ≈C_G due to the large BP capacitance ($C_{BP} > 50\ C_G$),[33] which is also the reason why the heterojunction region almost does not affect the conduction of each channel. Figure S3 (Supporting Information) shows the threshold voltages for holes and electrons in the BP channel are 10.2 and 15.7 V, respectively, and in the $MoTe_2$ channel are −49.8 and 5.2 V, respectively. To simplify the calculations, we treated both BP and $MoTe_2$ as nondegenerate semiconductors, and the Fermi level positions E_F were estimated by the following equations

$$E_F = \begin{cases} E_C + k_B T \ln \dfrac{n}{N_C} \\ E_V - k_B T \ln \dfrac{p}{N_V} \end{cases} \tag{2}$$

where n/p is the number of electrons/holes per unit volume, $N_{C/V} = 2(2\pi m^* k_B T/h^2)^{3/2}$ is the effective density of states in the conduction/valence band, m^* is the effective mass of the electron/hole, k_B is the Boltzmann constant, and T is the temperature (300 K, in this case). Figure S3 in the Supporting Information shows the values of n and p in BP and $MoTe_2$ under different gate voltages. Combined with the effective mass ($m_e^* = 0.42m_0, m_h^* = 0.26m_0$ for BP,[34,35] and $m_e^* = 0.55m_0, m_e^* = 0.67m_0$ for $MoTe_2$,[36] where m_0 is the mass of free electron in vacuum), the effective density of states in the conduction band and valence band are $N_C = 6.8 \times 10^{18}$ cm^{-3} and $N_V = 3.31 \times 10^{18}$ cm^{-3} for BP, and $N_C = 1.02 \times 10^{19}$ cm^{-3} and $N_V = 1.37 \times 10^{19}$ cm^{-3} for $MoTe_2$, respectively. The Fermi level positions of the BP and $MoTe_2$ layers at different gate voltages were then calculated as shown in Figure 1e,f. At V_G = −60, 0, and 60 V, the Fermi level positions of the BP($MoTe_2$) are −4.4, −4.35, −4.13 eV (−4.5, −3.96, −3.85 eV), respectively. According to the energy band diagram in Figure 1c, the intrinsic Fermi level positions (E_i) of BP and $MoTe_2$ are both about −4.25 eV. The intersections of the fitted curves and E_i corresponds to the neutral point of the ambipolar transfer curves. From the results, the neutral points for BP and $MoTe_2$ are $V_G \approx 15$ V and $V_G \approx -35$ V, respectively.

To investigate the properties of the built-in electric field in different configurations (p-P, p-N, and n-N type), we measured the electrical characteristics over the heterojunction between electrodes D1 (in contact with BP) and S1 (in contact with $MoTe_2$) under different gate voltages, as shown in **Figure 2**a. According to the device structure, the transport properties of the BP/$MoTe_2$ heterojunction device are mainly affected by the Au–BP and Au–$MoTe_2$ contacts, the BP and $MoTe_2$ channel conductance, and the BP/$MoTe_2$ heterojunction. The Au–BP and Au–$MoTe_2$ contacts were confirmed as ohmic contacts, as shown in Figure S4 (Supporting Information), indicating that the rectification effect of metal–semiconductor contacts can be safely ignored. Consequently, the rectification characteristic of the device is dominantly by the built-in electric field of the BP/$MoTe_2$ heterojunction. As shown in Figure 2a, the I_D–V_D curves of the device show remarkably different rectification properties under different V_G. To further clearly show that, we plot the forward current I_F under $V_D = 1$ V, the reverse current I_R under $V_D = -1$ V, and the rectification ratio I_F/I_R at different V_G, as shown in Figure 2b. When V_D varies from −30 to 10 V, the BP layer and $MoTe_2$ layer maintain their intrinsic doping types as p-type and N-type, respectively. The p-N type BP/$MoTe_2$ heterojunction exhibits strong current rectification property with a rectification ratio of up to 10^3, which is consistent with p-N type van der Waals heterojunctions reported previously.[26,37,38] When $V_G \geq 20$ V, the BP layer becomes n-type doped. The BP/$MoTe_2$ heterojunction trends to n-N type and the rectification ratio drops by an order of magnitude. For the cases of $V_G \leq -40$ V, both the BP layer and $MoTe_2$ layer are p-doped, and the BP/$MoTe_2$ heterojunction tunes to p-P type. The I_D–V_D curves of p-P type BP/$MoTe_2$ heterojunction show obvious symmetric linear conductivity behavior, and the rectification ratio is close to 1.

The different rectification properties in the three configurations of the BP/$MoTe_2$ heterojunction can be attributed to the difference of the built-in electric field, which can be

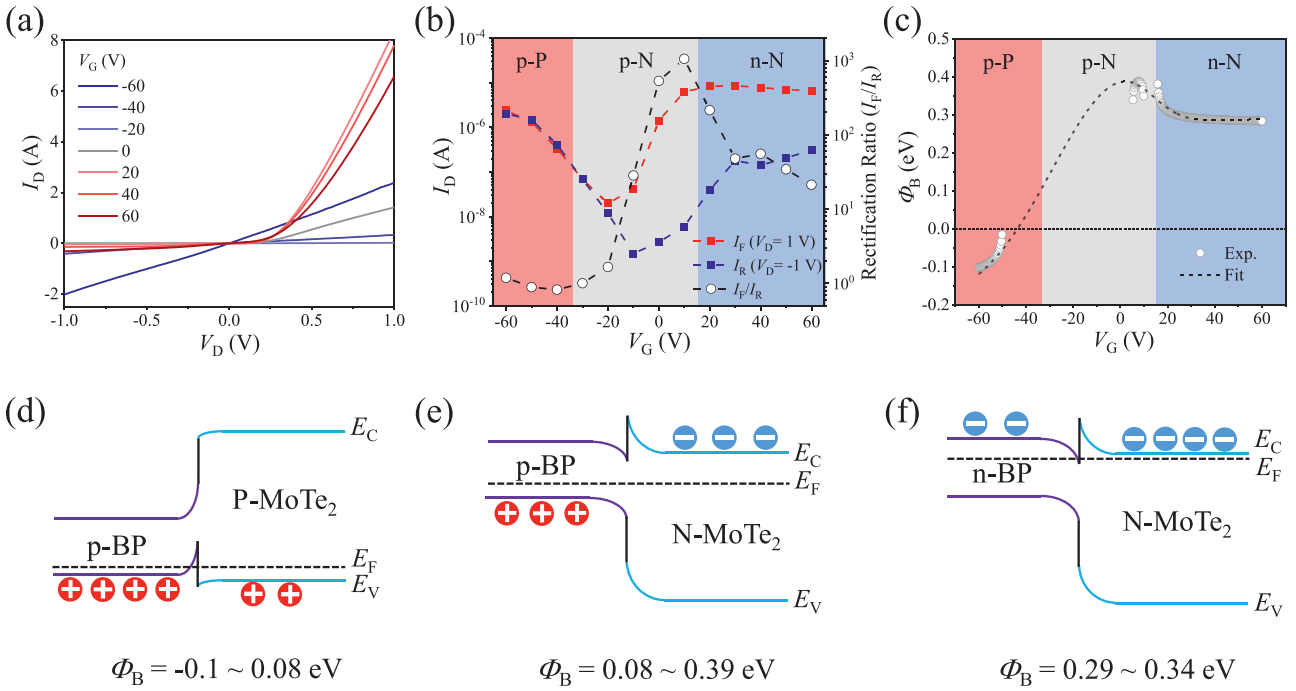

Figure 2. a) Current–voltage (I_D–V_D) curves of the BP/$MoTe_2$ heterojunction at different gate voltages under dark condition (measured between contacts D1 and S1). b) Forward current, reverse current, and rectification ratio versus V_G in semi-log scale, corresponding to three types of heterojunction configurations. c) Gate-dependent built-in electric potential of the BP/$MoTe_2$ heterojunction. Negative values mean that the direction of the built-in electric field is reversed. Dotted line represents the difference between the fitted curves in Figure 1e and f. Equilibrium energy band diagrams of d) p-BP/P-$MoTe_2$, e) p-BP/N-$MoTe_2$, and f) n-BP/N-$MoTe_2$ heterojunctions.

simply estimated by the built-in electric potential Φ_B of the heterojunction

$$\Phi_B = E_F(MoTe_2) - E_F(BP) \quad (3)$$

where E_F(BP) and E_F($MoTe_2$) are the Fermi level positions of BP and $MoTe_2$ layers shown in Figure 1e,f, respectively. The calculated values of the built-in electric potential Φ_B in the BP/$MoTe_2$ heterojunction under different gate voltages are depicted in Figure 2c. It is well known that the built-in potential of the heterojunction is proportional to the rectification ratio. For anisotype (p-N) heterojunction (gate voltage in the range from −35 to 15 V), the Φ_B varies from 0.08 to 0.39 eV (the maximum value obtained at V_G = 9.6 V), which is consistent with the maximum rectification ratio at V_G = 10 V in Figure 2b. Three configurations can also be illustrated with the band structure, as sketched in Figure 2d–f. For p-P type as V_G increases from −60 to −35 V, the built-in potential varies from −0.1 to 0.08 eV. The small built-in potential in the p-P type heterojunction results in a weak rectification effect. As V_G increases from −35 to 15 V, the Fermi level of the heterojunction approaches the valence band of BP and the conduction band of $MoTe_2$, leading to a typical p-N heterojunction. With the further increase of V_G from 15 to 60 V, the Fermi level approaches the conduction bands of both BP and $MoTe_2$, forming an n-N heterojunction. The rectification ratio is lowered but still in one order because of the large built-in electric potential around 0.3 eV.

Determined by the gate-tunable band diagram and built-in electric field, various photovoltaic characteristics are expected from the different configurations of the BP/$MoTe_2$ heterojunction. The short-circuit current I_{SC} and open-circuit voltage V_{OC} are two important quantities especially relevant in the photovoltaic characteristics of the heterojunction, which are generated from the spontaneous separation of electron-hole pairs driven by the built-in electric field.[25–27] By focusing a laser with the wavelength of 532 nm onto the heterojunction, I_D–V_D curves under illumination in the gate range of −60 to 60 V are plotted in **Figure 3**a. As shown in the inset of Figure 3a, the I_{SC} has negative values and V_{OC} has positive values at V_G > −35 V but both decayed close to zero at V_G ≤ −35 V. The results are in good agreement with the different built-in electric field in three configurations (p-P, p-N, and n-N type) of the BP/$MoTe_2$ heterojunction shown in Figure 2. When V_G ≤ −35 V, the disappearance of the I_{SC} and V_{OC} can be attributed to the weak built-in electric field in the p-P heterojunction. However, when the heterojunction is tuned to p-N or n-N type at V_G > −35 V, the photogenerated electron-hole pairs are separated by the strong built-in electric field to produce the short-circuit current I_{SC} and the open-circuit voltage V_{OC}, as indicated by the colored squares in Figure 2e,f. With the decrease of built-in electric field decreases when V_G > 0 V, both I_{SC} and V_{OC} decrease accordingly.

To characterize the gate-switchable photovoltaic effect deeply, the dependence of the short-circuit current I_{SC} on the gate voltage is further examined by varying the laser incident power, as shown in Figure 3b. The photovoltaic effect in the BP/$MoTe_2$ heterojunction is considered to be turned "ON" at V_G > −35 V, where I_{SC} increases accordingly as the increased incident laser power P_{Laser}. When V_G = 0 V, the I_{SC} is higher

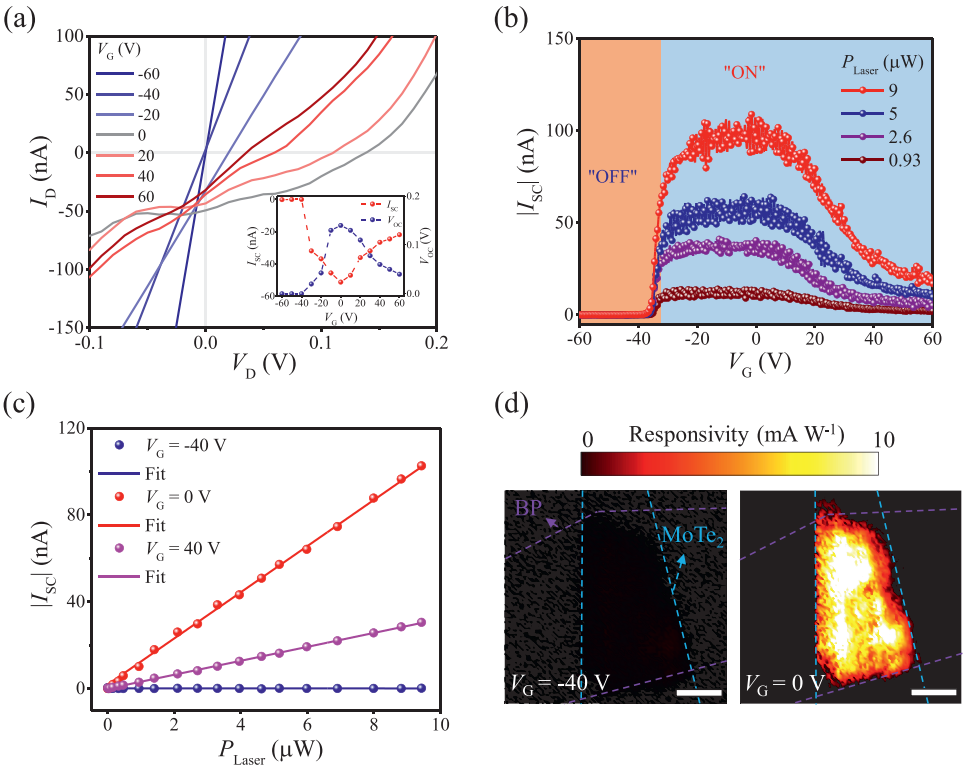

Figure 3. a) Current–voltage (I_D–V_D) curves at various gate voltages under 532 nm laser illumination. The inset is the short-circuit current I_{SC} and open-circuit voltage V_{OC} at different gate voltages. b) Short-circuit current I_{SC} as a function of gate voltages under varying incident laser power. The short-circuit current is switched to an "OFF" state when the BP/$MoTe_2$ heterojunction is turned to p-P type by gate voltages. c) Short-circuit current I_{SC} as a linear function of the incident laser power at V_G = –40, 0, 40 V. d) Photocurrent maps of the device presented in Figure 1b at V_G = –40 and 0 V with 532 nm laser excitation. The BP and $MoTe_2$ area are indicated by red and blue dashed lines, respectively. Scale bar, 3 μm.

than 100 nA with 9 μW incident power, and the photovoltaic responsivity R is estimated to be ≈10.8 mA W^{-1} by $R = I_{SC}/P_{Laser}$. However, the photovoltaic effect is turned "OFF" when $V_G \leq -35$ V, where the I_{SC} is less than 1 pA regardless of the laser power. The gate-switchable photovoltaic effect can also be depicted with the gate-dependent external quantum efficiency, as shown in Figure S5 (Supporting Information). Figure 3c shows I_{SC} as a function of P_{Laser} at V_G = –40, 0, 40 V. As can be seen from the good agreement between the fit and the experimental plots, the short-circuit current depends linearly on the incident power, which confirms the dominating mechanism of the photovoltaic effect. V_{OC} as a function of P_{Laser} is also shown in Figure S6 (Supporting Information). To verify the consistency of the gate-switchable photovoltaic effect in the entire heterojunction area, we performed the spatial mapping of I_{SC} in a home-built optical microscope. Figure 3d displays the photovoltaic current maps measured at V_G = 0 V and V_G = –40 V, respectively. A strong photoresponse is observed in the BP/$MoTe_2$ heterojunction area at V_G = 0 V, indicating spontaneous charge separation occurring at the heterojunction area. In contrast, the photovoltaic current is switched "OFF" in the entire junction region when V_G = –40 V. The uniformity of the photoresponse in the entire BP/$MoTe_2$ heterojunction region provides a scalable optical signal access area for the optoelectronic devices. Results of the other seven BP/$MoTe_2$ devices with different layer-thicknesses are shown in Figure S7 (Supporting Information), verifying the repeatability of the gate-switchable photovoltaic effect in BP/$MoTe_2$ heterojunction devices.

Based on the gate-switchable photovoltaic effect, we further develop a self-driven optoelectronic logic device based on the BP/$MoTe_2$ heterojunction, as schematically shown in **Figure 4**a. The device operates with an input signal (light) and a control signal (gate voltage) and yields an output signal (source-drain current), which is equivalent to the integration of a photodiode and a transmission gate. Figure 4b illustrates the operation conditions of the logic device in the form of I_D-V_G curves. The input signal is in the input-OFF state (represented by "0") when no light is shined on the device and it is in the input-ON state (represented by "1") when the device is illuminated with a 5 μW laser. The gate voltage is used as the control signal: control-OFF state ("0") for V_G = 0 V and control-ON state ("1") for V_G = –60 V. The output state of the device will depend on the source-drain current level of the device: output-OFF state ("0") for $I_D < 10^{-12}$ A and output-ON state ("1") for $I_D > 10^{-12}$ A. The logic device exhibits an output on/off ratio of up to 10^5 under a weak input signal and an ultra-low output dark current of <1 pA, which enables the applications in photoelectronic logic circuits with high performance and low power consumption. It should be noted that the gate voltage to control the optoelectronic logic device could be greatly reduced by using a high-κ dielectric layer or a thinner dielectric layer to improve modulation efficiency.[39,40] To test the parallel detection and processing functions of the self-driven optoelectronic logic device,

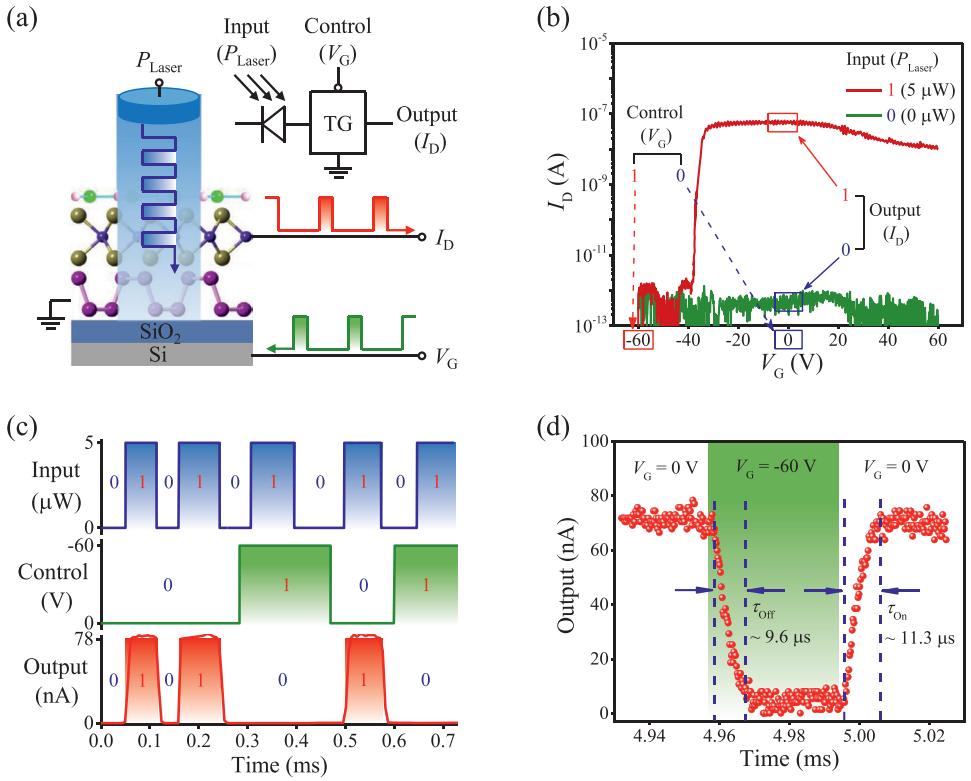

Figure 4. a) Schematic demonstration of the self-driven optoelectronic logic device based on the BP/$MoTe_2$ heterojunction, which is equivalent to the integration of a photodiode and a transmission gate. The gate voltage is used to logically control the optoelectronic conversion from the optical input to the electrical output. b) A typical set of operations determining the "0" and "1" logic states for input, control, and output conditions, as determined by the dark currents and photocurrents. c) Output of the self-driven optoelectronic logic device for different input and control logic states as a function of time. d) Output switch on/off time of the device, defined as the photocurrent increased/decreased from 10/90% to 90/10% of the stable photocurrent.

Figure 4c shows the typical time trace of the output state for different logic states of input and control. In the control OFF-state ("0") at $V_G = 0$ V, the input optical signal is converted into the electrical signal, and in the control ON-state ("1") at $V_G = -60$ V, the optical signal is shielded. The device realizes the functional integration and parallel operation of reading and decoding the input optical signal in the optoelectronic circuit.

The response times of optoelectronic logic devices reported elsewhere are in the order of seconds owing to the defects-related processes.[17,18,20] For the self-driven optoelectronic logic device demonstrated here, the switch time of the output photocurrent is determined by the photovoltaic process, which therefore promises a fast switching response. The photovoltaic response time τ_R of the BP/$MoTe_2$ heterojunction device can be described by

$$\tau_R = \sqrt{\tau_{Drift}^2 + \tau_{Diff}^2 + \tau_{RC}^2} \quad (4)$$

where τ_{Drift} is the drift time of photogenerated carriers in the heterojunction, τ_{Diff} is the diffusion time of photogenerated carriers in the BP and $MoTe_2$ channels, τ_{RC} is the equivalent circuit RC time constant of the heterojunction device. The existing study showed that the τ_{Drift} of photogenerated carriers in the built-in electric field region of the heterojunction can reach picosecond level.[41] From the dynamic operation results shown in Figure 4d, the turn-off and turn-on times of the output photocurrent are calculated as 9.6 and 11.3 μs, respectively. The time for switching the photovoltaic current is less than 10 μs, which can be further accelerated by reducing the length of the BP and $MoTe_2$ channels to shorten the τ_{Diff} and τ_{RC}.

To evaluate the performance of the demonstrated logic device based on the BP/$MoTe_2$ heterojunction, we compare the output dark current and switch time with those from the reported optoelectronic logic devices, as shown in **Figure 5**a. Because of the required external bias, dark currents of all those reported logic devices are at higher levels than the pA achieved in this work, which inevitably results in extra power consumption. Besides, the operations of optoelectronic logic in those devices were realized via the trapping and de-trapping of photo-induced carriers, which limits the response time significantly. In Figure 5a, our device is not the fastest but shows a potential logic switching speed. As a result, the self-driven BP/$MoTe_2$ heterojunction optoelectronic logic device exhibits high-performance with ultra-low output dark current and fast switching speed. In addition, the proposed BP/$MoTe_2$ heterojunction could respond to the optical illumination in a wide spectral range because of the narrow bandgap of the BP layer, enabling the broadband operation of the logic device. Figure 5b shows the wavelength-dependent photoresponsivity of the BP/$MoTe_2$ heterojunction in the ON- and OFF-states with the illumination of light in the range from 400 to 1600 nm, where the ON- and OFF-states are controlled by the gate voltage at 0 and –60 V, respectively. When $V_G = -60$ V, the light responsivity is lower than 10^{-6} A W^{-1}. The variable photoresponsivity

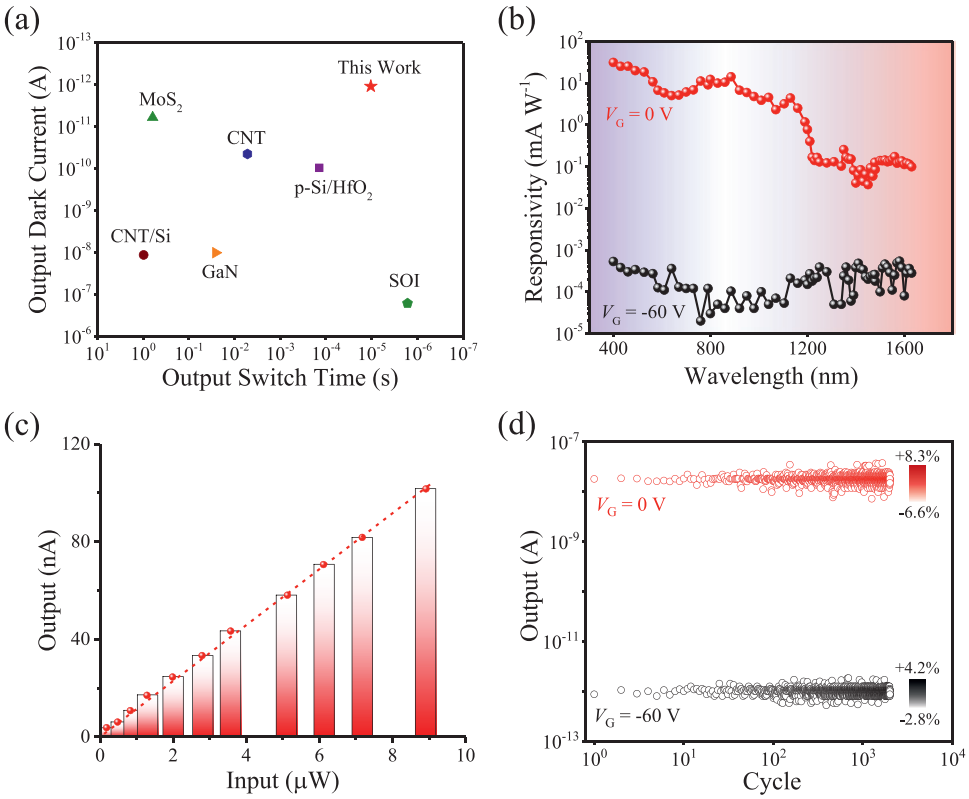

Figure 5. a) Comparison of output dark current and switch time of different optoelectronic logic devices made of SOI,[15] GaN,[16] CNT,[17] CNT/Si,[18] MoS_2,[21] and p-Si/HfO_2[43] that require external bias. b) Responsivities for input light at different wavelengths at $V_G = 0$ V and $V_G = -60$ V. c) Linear relationship between the output current and the input optical signal. d) Cycling tests of the output currents at $V_G = 0$ V and $V_G = -60$ V. Red and black color bars present deviation from the average value of the output currents.

is caused by bad signal-to-noise ratio at OFF-state, and measurement errors as well. The large responsivity difference between the ON- and OFF-states at different laser wavelengths implies the optoelectronic logic device could also support the wavelength multiplexing in a wide spectral range of the input optical signal.

Another figure of merits of an optoelectronic logic device is the linear response on the "input" signal strength. Due to the photovoltaic effect of BP/$MoTe_2$ heterojunction, the output photocurrent is indeed linearly dependent on the input optical power, as shown in Figure 5c. Owing to the highly linear response of output current signal, the "optical input-electronic output" logic gate is capable of multilevel operation by using a single optical pulse with different light intensities. We also test the repeatability of the switching ON/OFF process, as shown in Figure 5d. By switching the V_G between 0 and −60 V for 2000 cycles, the deviation from the average value of the output current for each cycle is less than 10%, indicating a highly reproducible switching logic operation. These decent characteristics of the BP/$MoTe_2$ optoelectronic logic device show its potential for practical applications.

3. Conclusion

In summary, we have successfully fabricated a van der Waals heterojunction device with BP and $MoTe_2$ 2D materials and demonstrated that the device can function as a high-performance self-driven optoelectronic logic device attributed to the gate-switchable photovoltaic effect. Specifically, an ultra-low output dark current less than 1 pA and an output current on/off ratio exceeding 10^5 are achieved at room temperature. More importantly, the self-driven optoelectronic logic device exhibits a wide selectable wavelength range of input optical signals and a linear relationship between the output current signal and the input optical signal. Based on the decent performance of the self-driven optoelectronic logic device, we believe that it offers great potential to develop future optoelectronic logic devices for high-performance and low-power-consumption optoelectronic circuits.

4. Experimental Section

Device Fabrication: The heterojunction of BP and $MoTe_2$ was achieved by a dry transfer method in a glove box (Ar atmosphere).[28] The bulk crystal of BP and $MoTe_2$ were purchased from HQ Graphene Corporation. First, a multilayer BP flake was mechanically exfoliated onto a PDMS film and transferred onto the SiO_2/Si substrate on a transfer platform equipped with a micromanipulator and a microscope. In the same way, the $MoTe_2$ flake was precisely transferred onto the surface of the BP flake to overlap at the middles of their channels. After the alignment to the proposed position, the PDMS film was pressed on the SiO_2/Si substrate about 3 min, then slowly lift up to transfer $MoTe_2$ onto the BP flake. 100 nm-thickness Au electrodes were prepared on a

silicon substrate using a shadow mask by thermal evaporation, which were then mechanically peeled off by PDMS and transferred onto the channel ends of both BP and $MoTe_2$ flakes.[42] Finally, an *h*-BN flake was transferred onto the heterojunction area to encapsulate the device.

Electrical and Optoelectronic Characterizations: The BP/$MoTe_2$ heterojunction device was first annealed in a tube furnace (BTF-1200C, BEQ) filled with inert gas (95% Ar and 5% H_2) at 200 °C for 2 h. The electrical transport characteristics of the fabricated devices were measured at room temperature in ambient. All the direct-current electrical characterizations were performed using a Keysight B2912A dual-channel digital source meter. The photocurrents of the heterojunction were measured in a home-built microscope. The incident laser was a supercontinuum laser equipped with an acousto-optic tunable filter for obtaining light with different wavelengths. The laser beam was focused by the objective lens and the spot size of the 532 nm laser was about 3 µm in diameter. A galvo-mirror system was employed for the spatial mapping of the photocurrent. The transient response of the device was measured by an oscilloscope (wavePro740Zi-A, LeCroy) with the gate voltage applied by a signal generator (AFG3101, Tektronix). The modulation of the laser was realized by a mechanical chopper.

Supporting Information

Supporting Information is available from the Wiley Online Library or from the author.

Acknowledgements

This project was primarily supported by the National Key R&D Program of China (Grant Nos. 2018YFA0307200 and 2017YFA0303800), the National Natural Science Foundation of China (Grant Nos. 61905198, 61775183, 11634010, and 61675171), Key Research and Development Program in Shaanxi Province of China (Grant Nos. 2017KJXX-12, 2018JM1058, and 2018KW-009), the Fundamental Research Funds for the Central Universities (Grant Nos. 3102017jc01001, 3102018jcc034, and 3102017HQZZ022).

Conflict of Interest

The authors declare no conflict of interest.

Keywords

gate-switchable devices, optoelectronic logic devices, photovoltaic effect, self-driven devices, van der Waals heterojunction

Received: October 18, 2020
Revised: November 27, 2020
Published online: December 18, 2020

[1] J. W. Goodman, F. I. Leonberger, S. Y. Kung, R. A. Athale, *Proc. IEEE* **1984**, *72*, 850.
[2] D. Fey, *Optik* **2001**, *112*, 274.
[3] A. F. Benner, M. Ignatowski, J. A. Kash, D. M. Kuchta, M. B. Ritter, *IBM J. Res. Dev.* **2005**, *49*, 755.
[4] M. A. Taubenblatt, *J. Lightwave Technol.* **2012**, *30*, 448.
[5] M. Kaba, M. Mallet, L. Pujol, C. Claudepierre, J. Veyron, R. Giroud, D. Mouseaux, F. Quentel, V. Foucal, M. M. Pez, in *Adv. Free-Space Opt. Commun. Tech. Appl. III, Proc. SPIE* **2017**, *10437*, 1043702.
[6] A. V. Krishnamoorthy, D. A. B. Miller, *Conf. Proc. Lasers Electro-Optics Soc. Annu. Meet.* **1996**, *1*, 340.
[7] V. G. Krasilenko, K. V. Ogorodnik, A. I. Nikolskyy, V. N. Dubchak, in *Int. Conf. Appl. Opt. Photonics, Proc. SPIE* **2011**, *8001*, 80012Q.
[8] S. L. Pyshkin, J. M. Ballato, *Optoelectronics: advanced materials and devices*, IntechOpen **2013**.
[9] V. G. Krasilenko, A. I. Nikolsky, A. A. Lazarev, S. N. Pavlov, in *Photonics Appl. Ind. Res. IV, Proc. SPIE* **2005**, *5948*, 59481G.
[10] V. G. Krasilenko, A. I. Nikolskyy, A. A. Lazarev, T. E. Magas, in *Inf. Opt. Data Storage II, Proc. SPIE* **2012**, *8559*, 85590K.
[11] S. Assefa, S. Shank, W. Green, M. Khater, E. Kiewra, C. Reinholm, S. Kamlapurkar, A. Rylyakov, C. Schow, F. Horst, H. Pan, T. Topuria, P. Rice, D. M. Gill, J. Rosenberg, T. Barwicz, M. Yang, J. Proesel, J. Hofrichter, B. Offrein, X. Gu, W. Haensch, J. Ellis-Monaghan, Y. Vlasov, in *2012 Int. Electron Devices Meet., IEEE* **2012**, 33.8.1.
[12] D. Fey, W. Erhard, M. Gruber, J. Jahns, H. Bartelt, G. Grimm, L. Hqppe, S. Sinzinger, *Proc. IEEE* **2000**, *88*, 838.
[13] M. P. Y. Desmulliez, *Mater. Sci. Eng., B* **2000**, *74*, 269.
[14] K. Wang, A. Nirmalathas, C. Lim, E. Wong, K. Alameh, H. Li, E. Skafidas, *Opt. Lett.* **2018**, *43*, 3132.
[15] D. Abraham, A. Chelly, J. Shappir, Z. Zalevsky, *Photonics Nanostruct. - Fundam. Appl.* **2011**, *9*, 35.
[16] X. Wang, Y. Zhang, X. Chen, M. He, C. Liu, Y. Yin, X. Zou, S. Li, *Nanoscale* **2014**, *6*, 12009.
[17] Y. Liu, S. Wang, H. Liu, L. Peng, *Nat. Commun.* **2017**, *8*, 15649.
[18] Y. L. Kim, H. Y. Jung, S. Park, B. Li, F. Liu, J. Hao, Y. K. Kwon, Y. J. Jung, S. Kar, *Nat. Photonics* **2014**, *8*, 239.
[19] H. Fang, W. Hu, *Adv. Sci.* **2017**, *4*, 1700323.
[20] K. Roy, M. Padmanabhan, S. Goswami, T. P. Sai, G. Ramalingam, S. Raghavan, A. Ghosh, *Nat. Nanotechnol.* **2013**, *8*, 826.
[21] C. Liu, H. Chen, X. Hou, H. Zhang, J. Han, Y. G. Jiang, X. Zeng, D. W. Zhang, P. Zhou, *Nat. Nanotechnol.* **2019**, *14*, 662.
[22] L. Li, Y. Yu, G. J. Ye, Q. Ge, X. Ou, H. Wu, D. Feng, X. H. Chen, Y. Zhang, *Nat. Nanotechnol.* **2014**, *9*, 372.
[23] D. Qu, X. Liu, M. Huang, C. Lee, F. Ahmed, H. Kim, R. S. Ruoff, J. Hone, W. J. Yoo, *Adv. Mater.* **2017**, *29*, 1606433.
[24] Y. Hassan, P. K. Srivastava, B. Singh, M. S. Abbas, F. Ali, W. J. Yoo, C. Lee, *ACS Appl. Mater. Interfaces* **2020**, *12*, 14119.
[25] W. J. Yu, Y. Liu, H. Zhou, A. Yin, Z. Li, Y. Huang, X. Duan, *Nat. Nanotechnol.* **2013**, *8*, 952.
[26] C. H. Lee, G. H. Lee, A. M. Van Der Zande, W. Chen, Y. Li, M. Han, X. Cui, G. Arefe, C. Nuckolls, T. F. Heinz, J. Guo, J. Hone, P. Kim, *Nat. Nanotechnol.* **2014**, *9*, 676.
[27] M. Long, E. Liu, P. Wang, A. Gao, H. Xia, W. Luo, B. Wang, J. Zeng, Y. Fu, K. Xu, W. Zhou, Y. Lv, S. Yao, M. Lu, Y. Chen, Z. Ni, Y. You, X. Zhang, S. Qin, Y. Shi, W. Hu, D. Xing, F. Miao, *Nano Lett.* **2016**, *16*, 2254.
[28] A. Castellanos-Gomez, M. Buscema, R. Molenaar, V. Singh, L. Janssen, H. S. J. van der Zant, G. A. Steele, *2D Mater.* **2014**, *1*, 011002.
[29] R. A. Doganov, E. C. T. O'Farrell, S. P. Koenig, Y. Yeo, A. Ziletti, A. Carvalho, D. K. Campbell, D. F. Coker, K. Watanabe, T. Taniguchi, A. H. C. Neto, B. Özyilmaz, *Nat. Commun.* **2015**, *6*, 6647.
[30] J. Kang, S. Tongay, J. Zhou, J. Li, J. Wu, *Appl. Phys. Lett.* **2013**, *102*, 012111.
[31] G. Zhang, S. Huang, A. Chaves, C. Song, V. O. Özçelik, T. Low, H. Yan, *Nat. Commun.* **2017**, *8*, 14071.
[32] A. Ortiz-Conde, F. J. García Sánchez, J. J. Liou, A. Cerdeira, M. Estrada, Y. Yue, *Microelectron. Reliab.* **2002**, *42*, 583.
[33] X. Chen, L. Wang, Y. Wu, H. Gao, Y. Wu, G. Qin, Z. Wu, Y. Han, S. Xu, T. Han, W. Ye, J. Lin, G. Long, Y. He, Y. Cai, W. Ren, N. Wang, *2D Mater.* **2016**, *3*, 015012.
[34] F. Yang, Z. Zhang, N. Z. Wang, G. J. Ye, W. Lou, X. Zhou, K. Watanabe, T. Taniguchi, K. Chang, X. H. Chen, Y. Zhang, *Nano Lett.* **2018**, *18*, 6611.

[35] G. Long, D. Maryenko, J. Shen, S. Xu, J. Hou, Z. Wu, W. K. Wong, T. Han, J. Lin, Y. Cai, R. Lortz, N. Wang, *Nano Lett.* **2016**, *16*, 7768.
[36] S. Das, A. Prakash, R. Salazar, J. Appenzeller, *ACS Nano* **2014**, *8*, 1681.
[37] P. Chen, T. T. Zhang, J. Zhang, J. Xiang, H. Yu, S. Wu, X. Lu, G. Wang, F. Wen, Z. Liu, R. Yang, D. Shi, G. Zhang, *Nanoscale* **2016**, *8*, 3254.
[38] Y. Xie, E. Wu, J. Zhang, X. Hu, D. Zhang, J. Liu, *ACS Appl. Mater. Interfaces* **2019**, *11*, 14215.
[39] M. Buscema, D. J. Groenendijk, G. A. Steele, H. S. J. Van Der Zant, A. Castellanos-Gomez, *Nat. Commun.* **2014**, *5*, 4651.
[40] M. Huang, S. Li, Z. Zhang, X. Xiong, X. Li, Y. Wu, *Nat. Nanotechnol.* **2017**, *12*, 1148.
[41] M. H. Doan, Y. Jin, S. Adhikari, S. Lee, J. Zhao, S. C. Lim, Y. H. Lee, *ACS Nano* **2017**, *11*, 3832.
[42] Y. Liu, J. Guo, E. Zhu, L. Liao, S. J. Lee, M. Ding, I. Shakir, V. Gambin, Y. Huang, X. Duan, *Nature* **2018**, *557*, 696.
[43] Y. Chen, S. Zhu, Q. Wei, Y. Xia, A. Li, J. Yin, Z. Liu, *Appl. Phys. Lett.* **2018**, *112*, 063503.